



Catalytic decomposition of gaseous ozone over manganese dioxides with different crystal structures



Jingbo Jia^{a,b}, Pengyi Zhang^{a,b,*}, Long Chen^c

^a State Key Joint Laboratory of Environment Simulation and Pollution Control, School of Environment, Tsinghua University, Beijing 100084, China

^b Collaborative Innovation Center for Regional Environmental Quality, China

^c The State Key Laboratory for Advanced Metals and Materials, University of Science and Technology Beijing, Beijing 100083, China

ARTICLE INFO

Article history:

Received 13 November 2015

Received in revised form 20 January 2016

Accepted 24 February 2016

Available online 27 February 2016

Keywords:

Manganese dioxide

Crystal structure

Ozone decomposition

Raman spectroscopy

Peroxide

ABSTRACT

Ozone is a ubiquitous pollutant and manganese dioxide (MnO_2) has been widely used for ozone decomposition. However, the effect of MnO_2 structure on ozone decomposition has never been investigated. Three tunnel-structure polymorphs, i.e., α -, β - and γ - MnO_2 were prepared and characterized by BET, TEM, XRD, H_2 -TPR, O_2 -TPD, NH_3 -TPD, TGA-MS and XPS. The activity of three MnO_2 polymorphs for ozone decomposition followed the order of α -> γ -> β - MnO_2 . The α - MnO_2 owned the largest specific surface area and lowest average oxidation state of Mn. Furthermore, the adsorbed oxygen species on the surface of α - MnO_2 were more easily reduced. In-situ Raman spectroscopy results showed that peroxide species formed during ozone decomposition, and over α - MnO_2 they were more easily decomposed by increasing reaction temperature. It was found that the catalytic activity of MnO_2 strongly depended on the density of oxygen vacancies. Accordingly, the ozone decomposition mechanism based on the involvement and recycling of oxygen vacancy (V_O) is proposed. The decomposition of peroxide species is a rate-limiting step. These findings are helpful for designing more effective catalyst for ozone removal.

© 2016 Elsevier B.V. All rights reserved.

1. Introduction

Tropospheric ozone is a secondary air pollutant formed via the photochemical reactions of anthropogenic primary pollutants involving nitrogen oxides (NO_x) and volatile organic compounds (VOCs) driven by sunlight [1]. Exposure to high concentration ozone causes detrimental effect on human health including pulmonary function and airway inflammation [2], blood pressure [3], premature mortality [4], and reduces yields of staple crops [5]. Moreover, tropospheric ozone itself acts as a greenhouse gas and therefore contributes to global warming [6].

Most people spend the majority of their time indoors, so much of their exposure to ozone actually occurs inside buildings. The dominant source of indoor ozone is ambient ozone that penetrates indoors [7]. Besides, several kinds of indoor equipment involved high voltage discharge, electrostatic discharge or ultraviolet light irradiation (such as photocopiers, air-condition, sterilizer, etc.) contribute to elevated indoor ozone levels. Several

investigations have shown that indoor ozone can trigger secondary reactions and some known byproducts of these reactions include formaldehyde, organic acids and ultrafine particles [8–11]. Besides, catalytic ozonation is widely employed in low-temperature oxidation of volatile organic compounds (VOCs) in gas phase especially at low levels [12–19]. Usually the concentration of ozone in the off-gas from the process is well above the allowable values.

Catalytic materials explored for eliminating O_3 include noble-metal [20], various transition metal oxides supported on Al_2O_3 [21–23], SiO_2 , TiO_2 , activated carbon [24–28], cordierite [29] and zeolite [19,30–32]. Among them, manganese oxides especially MnO_2 is most frequently studied. Oyama and co-workers [33,34] examined the effect of supports on the ozone decomposition activity and found that difference in the structure of the manganese active center was the origin of support effect on the activity. However, XRD analysis indicated that supported manganese oxide was a well dispersed species when the MnO_2 loading was low and the information on the crystal structure was not given [28]. Raman spectra merely indicated that the component of manganese oxide catalysts was one or more of Mn_3O_4 , MnO_2 , Mn_2O_3 and MnO [22,27,33]. Therefore the relationship between structure of manganese oxides and their catalytic property for ozone decomposition is not clear. Only a few work have investigated the activity of manganese dioxides with specific crystal phase [35,36].

* Corresponding author at: State Key Joint Laboratory of Environment Simulation and Pollution Control, School of Environment, Tsinghua University, Beijing 100084, China.

E-mail address: zpy@tsinghua.edu.cn (P. Zhang).

To learn the effect of crystal structure of MnO_2 on their activity for ozone decomposition and the essential influencing factors, three tunnel-structure polymorphs of MnO_2 , i.e., α -, β - and γ - MnO_2 were prepared and tested for ozone decomposition in this study. It was found that α - MnO_2 had the highest activity, and the structure, morphology and redox properties of catalysts were characterized to illustrate the key factors influencing the ozone decomposition.

2. Experimental

2.1. Preparation of MnO_2 polymorphs

All chemicals were of analytical grade. α -, β - and γ - MnO_2 were synthesized by hydrothermal method as described in the literature [37]. Briefly, α - MnO_2 was synthesized by the hydrothermal reaction between KMnO_4 and $\text{Mn}(\text{Ac})_2$ at 140°C for 2 h. β - MnO_2 and γ - MnO_2 were prepared via the hydrothermal reaction between $(\text{NH}_4)_2\text{S}_2\text{O}_8$ and $\text{MnSO}_4 \cdot \text{H}_2\text{O}$ at 140°C for 12 h, and at 90°C for 24 h, respectively.

After the hydrothermal reaction, the resultant precipitates were filtered, washed and dried at 85°C in air for 12 h. All the samples were compressed, crushed and sieved through 40–60 mesh sieves before the activity evaluation.

2.2. Characterization

The crystal structure of as-prepared samples was verified by X-ray diffractometer (XRD, O8 discover, Siemens) equipped with $\text{Cu K}\alpha$ radiation at accelerating voltage and current of 40 kV and 40 mA, respectively. The specific surface areas of the catalysts were determined from N_2 adsorption/desorption analysis at 77 K with a QuadraSorb SI (Quantachrome). The samples were first degassed at 300°C for 4 h before measurement. The specific surface areas were determined by BET equation in 0.09–0.3 partial pressure range.

The morphology was observed with FE-SEM (S-5500, Hitachi) and HRTEM (Tecnai G2 F30 S-TWIN). The chemical state of Mn and O was determined by X-ray photoelectron spectroscopy (XPS, Thermo ESCALAB250xi). TGA was performed with STA 449 F3 Jupiter® (NETZSCH) at a heating rate of $10^\circ\text{C}/\text{min}$ from 50°C to 950°C and the evolved gas was analyzed by mass spectrometry (QMS 403C, NETZSCH).

H_2 -TPR profiles were recorded with AutoChemII 2920 (Micromeritics). 40 mg sample was placed in U-shaped quartz tube, heated to 105°C and purged with helium gas (He) for 0.5 h and then reduced in the stream of a mixture of 5% H_2/Ar (50 mL/min) at a heating rate of $5^\circ\text{C}/\text{min}$ to 600°C . The H_2 consumption was monitored by a thermal conductivity detector (TCD). For O_2 -TPD analysis, 80 mg sample was placed in U-shaped quartz tube, heated to 105°C and purged with He for 0.5 h to remove surface H_2O . After that, the catalyst was purged with a mixture of O_2/He (50/10 mL/min) at 25°C for 0.5 h. Desorption of O_2 was carried out from 25°C to 950°C at a heating rate of $5^\circ\text{C}/\text{min}$ purged with He. For NH_3 -TPD analysis, 100 mg catalyst was placed in U-shaped quartz tube, heated to 300°C and then purged with He for 1 h. After that, the catalyst was purged with 10% NH_3/He for 0.5 h at 100°C . Desorption of NH_3 was carried out from 100°C to 450°C at a heating rate of $10^\circ\text{C}/\text{min}$ in He, and then the temperature was maintained at 450°C for 1 h to achieve complete desorption.

2.3. Catalytic activity test

The activity of as-synthesized samples for ozone decomposition was carried out in a flow-through quartz tube reactor (ϕ 6 mm) using 0.1 g of catalyst with size of 40–60 mesh at different temperatures and relative humidity $\sim 1\%$. O_3 was generated by passing filtered clean air through a low-pressure mercury ultraviolet lamp

(10 V/3 W, Guangdong cnlight technology company). The total flow rate through the reactor was maintained at 1.1 L/min using mass-flow meters and included ~ 14 ppm O_3 balanced with clean air. The ozone concentration was determined with an ozone analyzer (Model 49i, Thermo Scientific, USA). The weight space velocity was set at $660 \text{ L g}^{-1} \text{ h}^{-1}$. The conversion was calculated from the proportion of inlet and outlet concentrations of ozone after 2 h reaction.

2.4. Ozone decomposition intermediates analysis

In-situ Raman spectroscopy was used to directly observe and identify intermediates during ozone decomposition. The in situ Raman spectra was recorded on a Renishaw inVia Raman Microscope with resolution of 2 cm^{-1} . The excitation source was an argon-ion laser at the wavelength of 532 nm. The CCR1000 catalyst cell reactor system (Linkam scientific instruments) was used to obtain continuous Raman spectrum under controlled temperature and flow rate of reactant stream. The catalyst of ~ 60 mg was pressed into thin wafer and mounted on a virtually unreactive disposable ceramic fabric filters placed inside the ceramic heating element. The temperature was accurately controlled by the T95 controller via the S-type platinum/rhodium thermocouple. The ozone was generated by passing pure oxygen through an electric field discharge ozone generator (Tonglin Technology) and the inlet ozone concentration was about 800 ppm. Spectra was acquired under oxygen flow and under ozone/oxygen mixture flow at different temperature.

3. Results and discussion

3.1. Crystal structure and textural properties

Fig. 1 shows the XRD patterns of as-prepared catalysts, which correspond well to α - MnO_2 (JCPDS 44-0141), β - MnO_2 (JCPDS 24-0735) and γ - MnO_2 (JCPDS 17-0510), respectively. The XRD patterns indicate that as-prepared catalysts are well crystallized and no

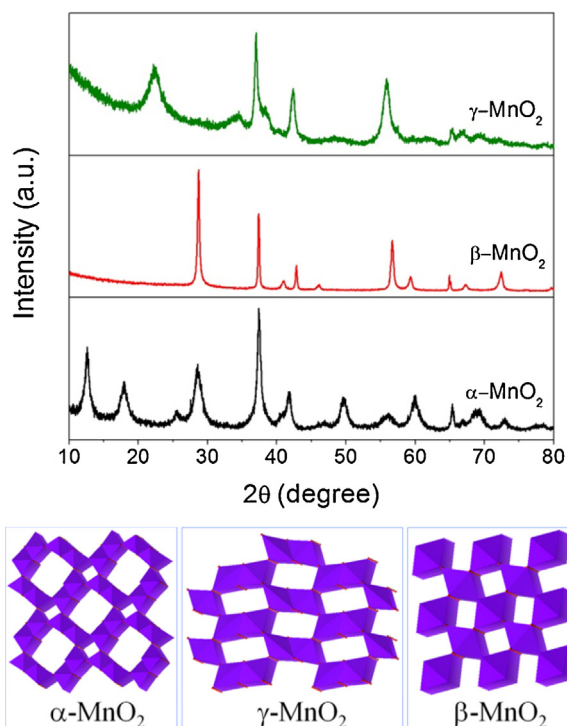


Fig. 1. XRD patterns and crystal structures of α -, β - and γ - MnO_2 .

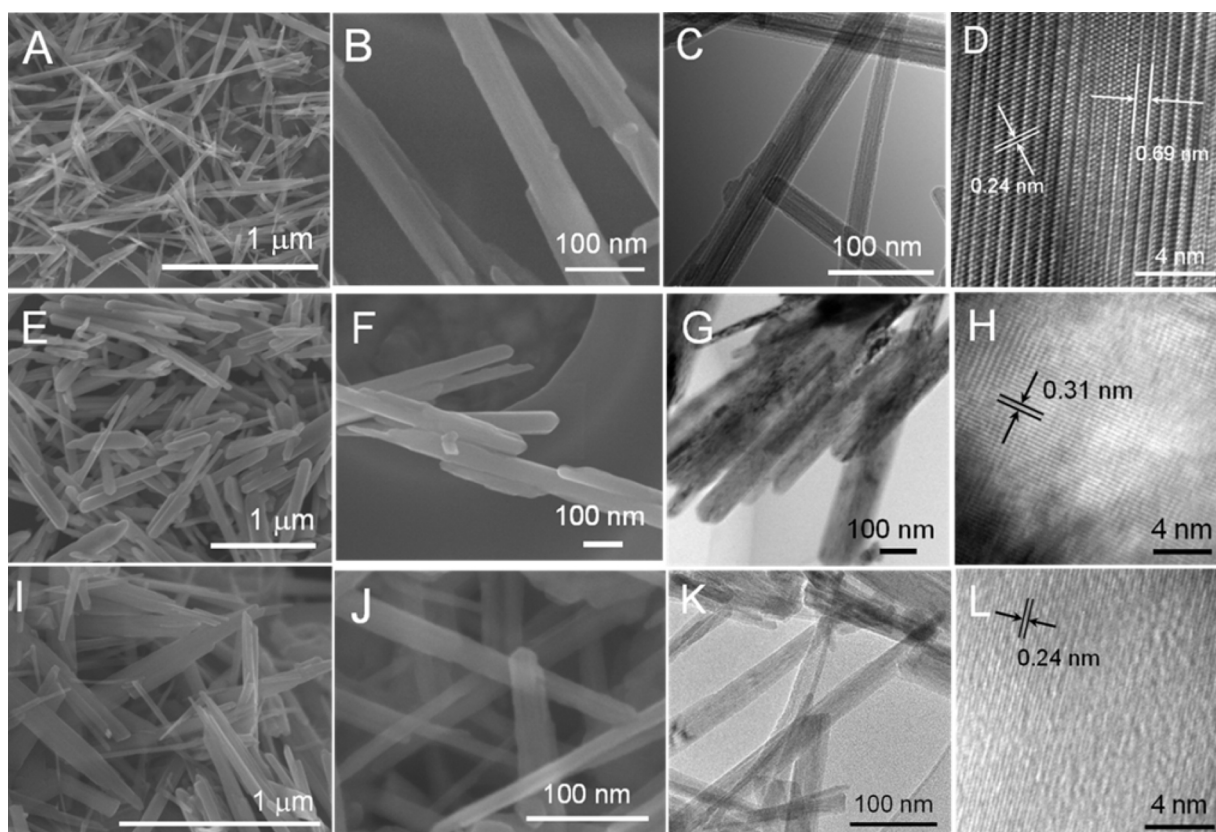


Fig. 2. SEM, TEM and HRTEM images of catalysts: (A–D) α - MnO_2 , (E–H) β - MnO_2 , (I–L) γ - MnO_2 .

Table 1
Specific surface area, H_2 -TPR data and NH_3 -TPD results.

Catalyst	Specific surface area ($\text{m}^2 \text{g}^{-1}$)	V_p ($\text{cm}^3 \text{g}^{-1}$)	H_2 consumption (mmol g^{-1})			Total acidity ($\mu\text{mol NH}_3 \text{g}^{-1}$)
			1st peak	2nd peak	Total	
α - MnO_2	80.7	0.35	3.26	4.83	8.09	82.0
β - MnO_2	13.8	0.028	7.59	3.41	11.0	20.6
γ - MnO_2	74.6	0.15	5.15	4.05	9.20	103

impurity phase could be detected. The structural variations of manganese oxides result from the different bonding ways of the basic MnO_6 octahedral units. Three MnO_2 polymorphs investigated in this study, i.e., α , β and γ - MnO_2 all own tunnel structure. Among them, α - MnO_2 possesses (2×2) tunnels with the size of $0.46 \text{ nm} \times 0.46 \text{ nm}$, β - MnO_2 displays (1×1) tunnels with the size of $0.23 \text{ nm} \times 0.23 \text{ nm}$, while γ - MnO_2 consists of (1×2) tunnels with the size of $0.46 \text{ nm} \times 0.23 \text{ nm}$ [38].

The morphologies and microstructures were observed by FE-SEM, TEM and HRTEM. As shown in Fig. 2(A and B), α - MnO_2 exhibits the morphology of interconnected nanofibers with diameters of 20–50 nm and lengths ranging from 100 nm to 2 μm . The TEM image in Fig. 2C displays the exact shape of nanofibers. Further from the HRTEM image in Fig. 2D, the lattice fringe spacings are about 0.24 nm and 0.69 nm with a cross angle of 59° , corresponding to the ($2\ 1\ 1$) and ($1\ 1\ 0$) planes of the tetragonal-structure α - MnO_2 , respectively. The SEM images in Fig. 2(E and F) and TEM image (Fig. 2G) show that their regular aggregation of short and thick β - MnO_2 nanofibers with diameters of 20–200 nm and lengths ranging from 100 nm to 1.5 μm . Similarly, the exposed facet of β - MnO_2 can be identified as the ($1\ 1\ 0$) plane with the lattice spacing of 0.31 nm (Fig. 2H). From the images in Fig. 2(I–K), the prepared γ - MnO_2 presents disorder aggregation of nanofibers with diameters of 10–20 nm and length of 200 nm to 1 μm . As indicated in Fig. 2L,

the lattice fringe with spacing of 0.24 nm corresponds to the ($2\ 2\ 0$) plane of γ - MnO_2 .

The BET specific surface areas of three MnO_2 polymorphs are given in Table 1. Among them, α - MnO_2 has the largest surface area ($80.7 \text{ m}^2 \text{g}^{-1}$), followed by γ - MnO_2 ($74.6 \text{ m}^2 \text{g}^{-1}$) and β - MnO_2 ($13.8 \text{ m}^2 \text{g}^{-1}$). Fig. S1 shows the N_2 adsorption/desorption isotherms and pore size distributions of α -, β - and γ - MnO_2 . All the catalysts exhibit a type IV isotherm with H3-type hysteresis rings, which indicate that they are mesoporous materials with non-uniform pores [39].

3.2. Temperature programmed studies

H_2 -TPR profiles (Fig. 3) of three MnO_2 were performed to evaluate their reducibility. The final reduction product of MnO_2 could be MnO with Mn_2O_3 and Mn_3O_4 as intermediates [40]. As for α - MnO_2 , two reduction peaks were observed at 308 and 318 $^\circ\text{C}$. As for γ - MnO_2 , the first reduction peak occurred at 331 $^\circ\text{C}$, and the second peak appeared at 442 $^\circ\text{C}$. The reduction pattern of β - MnO_2 was similar to γ - MnO_2 , but the peak position shifted to higher temperature, located at 362 and 464 $^\circ\text{C}$, respectively, indicating that β - MnO_2 was more difficult to be reduced by H_2 . The lower temperature of the first reduction peak means the easier reduction. According to the position of reduction peaks, the reducibility of three MnO_2 polymorphs decreases in sequence of α - $\text{MnO}_2 > \gamma$ -

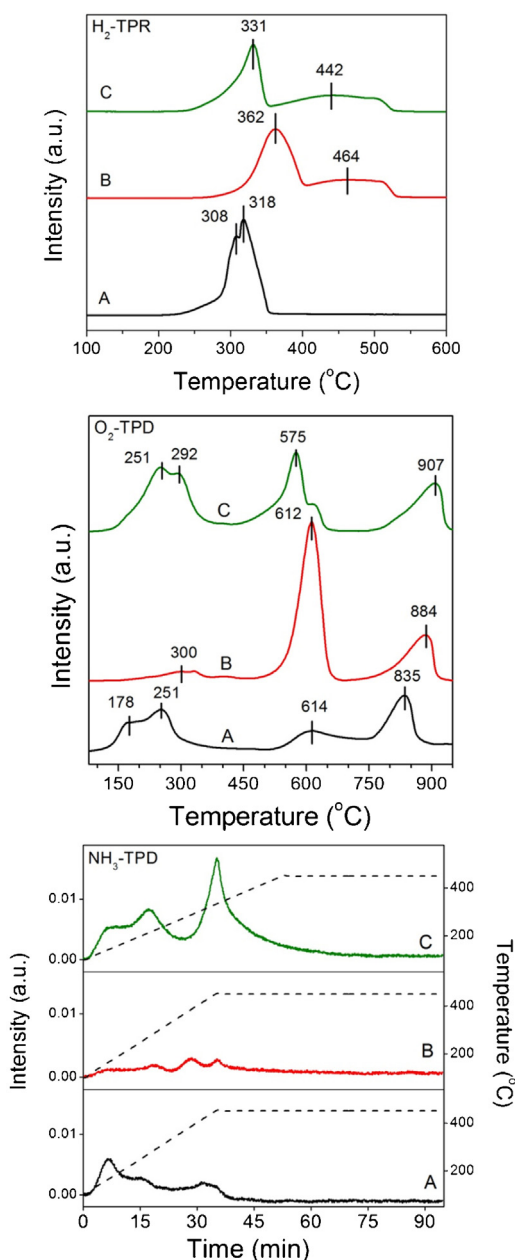


Fig. 3. H₂-TPR, O₂-TPD and NH₃-TPD profiles of catalysts: (A) α -MnO₂, (B) β -MnO₂, (C) γ -MnO₂.

MnO₂ > β -MnO₂. The amounts of consumed H₂ were calculated and listed in Table 1. Theoretically the H₂ consumption for the reduction of MnO₂ to Mn₃O₄ and Mn₃O₄ to MnO are 7.67 and 4.37 mmol/g, respectively; while the H₂ consumption for the complete reduction of MnO₂ to Mn₂O₃ and Mn₂O₃ to MnO are 5.74 and 6.33 mmol/g, respectively. As shown in Table 1, each H₂ consumption of three MnO₂ were somewhat lower than the theoretical amount of H₂ needed for reduction from MnO₂ to MnO, which indicates that a substantial fraction of Mn³⁺ exists in all MnO₂ samples [41,42].

Furthermore, O₂-TPD was conducted to investigate the evolution of oxygen (Fig. 3). The desorption peak below 350 °C can be ascribed to the release of chemisorbed oxygen molecules and active surface oxygen, while the peak in the range of 400–650 °C is attributed to the release of sub-surface lattice oxygen. The peak above 700 °C is due to the evolution of bulk lattice oxygen [43,44]. The lower temperature oxygen is released at, the looser this part of oxygen is bound to Mn atoms. As shown in Fig. 3, both α -MnO₂ and

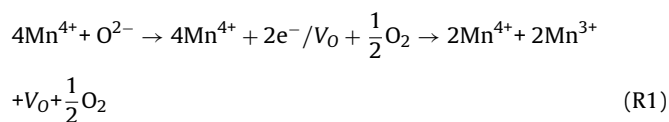
γ -MnO₂ contain abundant loosely bound surface oxygen species. However, little loosely bound surface oxygen species exist in β -MnO₂.

NH₃-TPD was adopted to determine the acidity of the three catalysts (Fig. 3). The amounts of acidic sites were estimated by integration of the area under the NH₃-TPD curve and the results are shown in Table 1. The peak position reflects the binding strength between NH₃ molecule and acid sites. Though γ -MnO₂ contains the largest amount of acidic sites, α -MnO₂ contains more weak acid sites than γ -MnO₂. It has been reported that the Mn cations on the exposed (1 1 0) plane in α -MnO₂ are 3 or 5 fold coordinated to oxygen, indicating that α -MnO₂ possesses many Lewis acidic sites, while all of the Mn cations on the exposed (1 1 0) plane of β -MnO₂ are located in the relatively saturated environment [45]. Thus, the different surface atomic configurations owned by MnO₂ polymorphs cause the difference in surface acidic sites.

The TGA profiles of the catalysts are presented in Fig. 4 and the evolved gas was simultaneously monitored by the mass spectrometry. The three MnO₂ polymorphs exhibit quite different thermal stability. The weight loss can be categorized into three segments. The initial weight loss below 120 °C can be attributed to the removal of physically adsorbed water. When the temperature rises from 120 °C to 350 °C, the corresponding weight loss can be ascribed to desorption of chemically bonded water and surface active oxygen species. The subsequent weight loss above 400 °C is due to the evolution of lattice oxygen and phase transformation from MnO₂ to Mn₂O₃ or Mn₃O₄ according to Fig. S2. Within β -MnO₂, the Mn and O atoms are almost stoichiometric coordinated, resulting in little adsorbed water in the framework. Thus in the TGA profile of β -MnO₂, no significant weight loss can be observed below 300 °C and only a small peak occurred at 311 °C, which is attributed to the removal of constitutional water. For α -MnO₂ and γ -MnO₂, both have the weight loss between 200 °C and 350 °C, which attribute to the removal of surface active oxygen, as confirmed by the mass spectroscopic detection. These results are consistent with those revealed by O₂-TPD above.

3.3. Surface atom state

Fig. 5 illustrates XPS spectra of Mn 2p_{3/2}, Mn 3s and O 1s. The Mn 2p_{3/2} spectra are deconvoluted into two peaks with binding energy at 641.9 and 642.8 eV ascribed to Mn³⁺ and Mn⁴⁺, respectively. A quantitative analysis on the molar ratios of surface Mn³⁺/Mn⁴⁺ is summarized in Table 2. The α -MnO₂ showed the highest surface Mn³⁺/Mn⁴⁺ molar ratio (0.76) whereas the β -MnO₂ exhibited the lowest (0.41), which is consistent with the H₂-TPR result. As we know, once Mn³⁺ appears in the manganese dioxide, oxygen vacancies will be generated to maintain electrostatic balance according to the following process (R1) [42]. So we can deduce that the surface oxygen vacancy density decreases in the order of α -MnO₂ > γ -MnO₂ > β -MnO₂.



where V_O represents an oxygen vacancy site.

Table 2
XPS results of surface Mn and O elements.

Catalyst	Mn 2p _{3/2}			Mn 3s	O 1s		
	Mn ³⁺ (%)	Mn ⁴⁺ (%)	Mn ³⁺ /Mn ⁴⁺	AOS of Mn	O _I (%)	O _{II} (%)	O _{II} /O _I
α -MnO ₂	43.3	56.7	0.76	3.63	64.1	35.9	0.56
β -MnO ₂	29.1	70.9	0.41	3.88	67.9	32.1	0.47
γ -MnO ₂	38.2	61.8	0.62	3.82	67.0	33.0	0.49

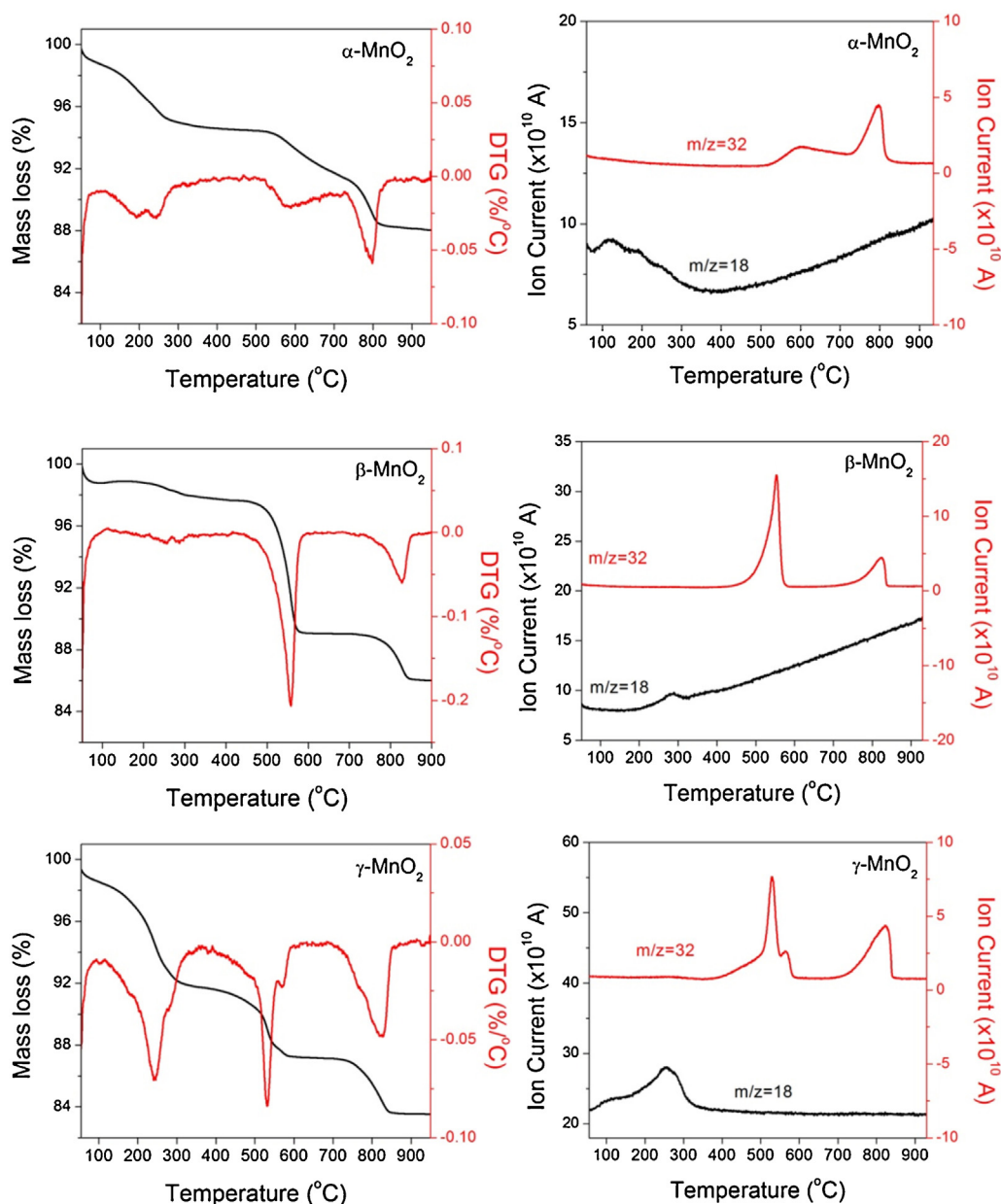


Fig. 4. TG/DTG-MS curves of catalysts.

The average oxidation state (AOS) of Mn was estimated based on the following formula: $\text{AOS} = 8.956 - 1.126 \Delta E_s$, where ΔE_s is the binding energy difference between the doublet Mn 3s peaks as shown in Fig. 5 [44]. The results show that the AOS decreases in the order of $\beta\text{-MnO}_2$ (3.88) > $\gamma\text{-MnO}_2$ (3.82) > $\alpha\text{-MnO}_2$ (3.63), which suggests that the fraction of Mn^{4+} in $\beta\text{-MnO}_2$ is the highest.

Two kinds of surface oxygen species can be distinguished by the O 1s spectra (Fig. 5). Lower binding energy of 529.5–529.7 eV can be ascribed to the lattice oxygen (O_I) and higher binding energy of 531.0–531.2 eV can be ascribed to the surface adsorbed oxygen (O_{II}). It can be seen from Table 2 that the O_{II}/O_I molar ratio decreases in sequence of $\alpha\text{-MnO}_2$ (0.56) > $\gamma\text{-MnO}_2$ (0.49) > $\beta\text{-MnO}_2$ (0.47). This result suggests that $\alpha\text{-MnO}_2$ has the most abundant surface adsorbed oxygen (O^{2-} , O^- , OH^-), which is consistent with its highest density of oxygen vacancies mentioned above, because usually oxygen molecules are adsorbed at the oxygen vacancies of an oxide material [42].

3.4. Catalytic activity

The activity for ozone decomposition was evaluated at different temperatures from 5 °C to 100 °C. As shown in Fig. 6, three MnO_2 polymorphs exhibit very different activities toward ozone decomposition, following the sequence of $\alpha\text{-MnO}_2$ > $\gamma\text{-MnO}_2$ > $\beta\text{-MnO}_2$. Among them, $\alpha\text{-MnO}_2$ presents the best performance, as the removal efficiency maintains at 100% during 120 min of reaction even at 5 °C. The other two catalysts, i.e., γ - and $\beta\text{-MnO}_2$ exhibit much lower activity with 100% ozone conversions achieved at 60 °C and 100 °C, respectively.

Fig. 7 shows the Arrhenius plots for ozone decomposition over the three MnO_2 polymorphs. According to the slopes of the Arrhenius plots, the apparent activation energies for ozone decomposition were calculated and summarized in Table 3. The apparent activation energy is 2.80 kJ/mol on $\alpha\text{-MnO}_2$, 8.13 kJ/mol on $\gamma\text{-MnO}_2$ and 15.2 kJ/mol on $\beta\text{-MnO}_2$, respectively. The apparent activation energy over $\alpha\text{-MnO}_2$ is the lowest, which indicates that surface

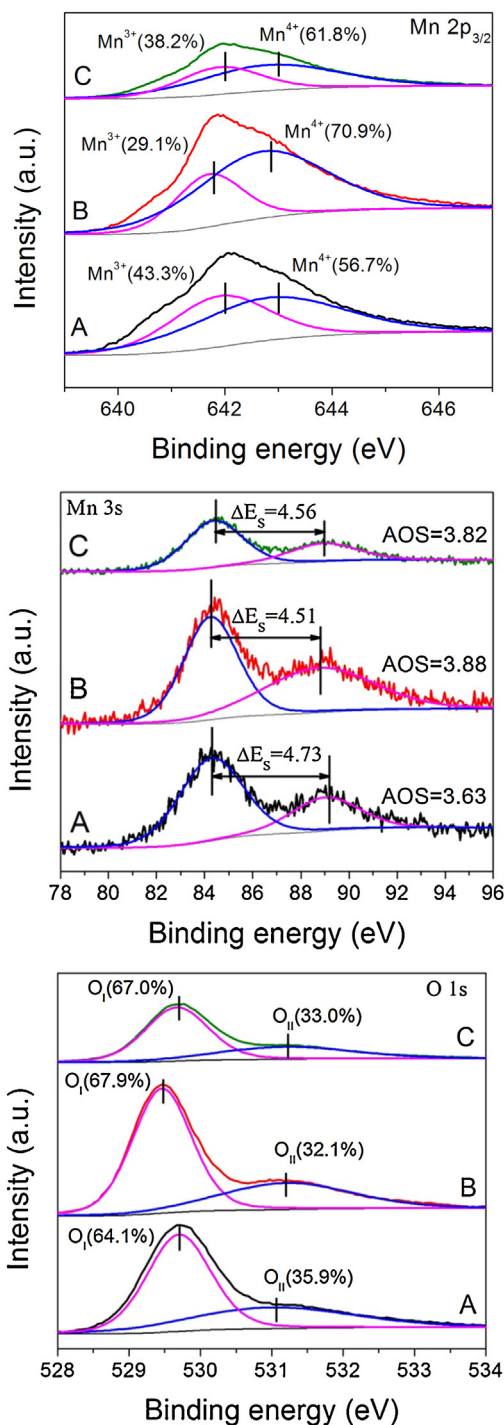


Fig. 5. Mn 2p_{3/2}, Mn 3s and O 1s XPS spectra of catalysts: (A) α -MnO₂, (B) β -MnO₂, (C) γ -MnO₂.

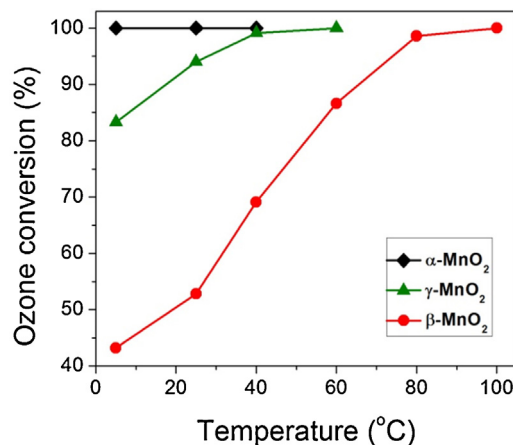


Fig. 6. Ozone conversion vs. temperature over α -, β - and γ -MnO₂ (ozone inlet concentration: 14 ppm, weight space velocity: 660 L g⁻¹ h⁻¹).

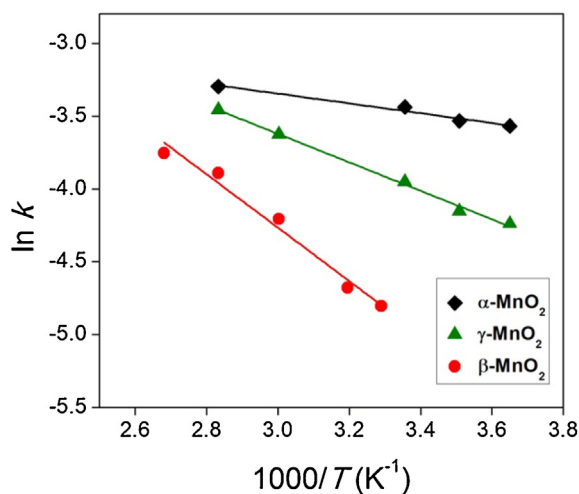


Fig. 7. Arrhenius plots for ozone decomposition over α -, β - and γ -MnO₂ (ozone inlet concentration: 90 ppm, catalyst weight: 20 mg).

of α -MnO₂ is most easily activated at low temperature. The reaction rate at 25 °C and the specific surface rate are also listed in Table 3. Though the overall reaction rate over β -MnO₂ is lowest, the corresponding specific surface reaction rate is about 3 times higher than those over α -MnO₂ and γ -MnO₂, which indicates the specific surface area is not the only factor determining the ozone decomposition.

The above results demonstrate that the catalytic activity of MnO₂ polymorph is tightly related to the crystal structure. Due to their own different tunnel structure, the average lengths of Mn-O bond in α -, β - and γ -MnO₂ are 0.198, 0.188 and 0.191 nm, respectively [40]. The longer length of Mn-O bond means it is more easily broken down. Luo et al. [46] reported that, some of oxygen atoms in the OMS-2 framework can easily escape from the framework without destroying the crystal structure, resulting in the formation of oxygen vacancies. As revealed by the above XPS analysis, the α -MnO₂ possessed the most abundant surface adsorbed oxygen

Table 3
Kinetic parameters of ozone decomposition over three catalysts.

Catalyst	E _a (kJ mol ⁻¹ J/mol)	Reaction rate at 25 °C (μg g ⁻¹ min ⁻¹)	Specific surface reaction rate (μg m ⁻² min ⁻¹)
α -MnO ₂	2.80	328	3.82
β -MnO ₂	15.2	163	11.8
γ -MnO ₂	8.13	290	3.88

species (relevant to the surface oxygen vacancy densities), which is in agreement with its highest catalytic activity. Thus, the catalytic activity of MnO_2 may be strongly related with its surface oxygen vacancies.

3.5. Ozone decomposition mechanism

It has been reported that the overall ozone decomposition process consists of the dissociative adsorption of ozone over the catalyst and then the decomposition of intermediate products. And active oxygen species are formed during ozone decomposition [22,33]. We used in-situ Raman spectroscopy to detect oxygen species over α -, β - and γ - MnO_2 catalysts exposed to oxygen and ozone/oxygen mixture at different temperatures, the results are shown in Fig. 8.

The signals located in the region of 500–700 cm^{-1} can be ascribed to the stretching vibrations of MnO_6 octahedral. For α - MnO_2 , the peaks located at 642 and 579 cm^{-1} belong to A_g spectroscopic species that originate from breathing vibrations of MnO_6 octahedra [47]. For β - MnO_2 , the bands of 665 and 534 cm^{-1} can be assigned to the A_{1g} and E_g mode, respectively [43]. For γ - MnO_2 , the band at 580 cm^{-1} is indicative of a well-developed orthorhombic structure with (1×2) tunnels [43,48].

When the α - MnO_2 is exposed to ozone/oxygen flow, a new peak at 835 cm^{-1} can be observed, indicating that new species form during ozone decomposition. According to the literature [49], the signal at 835 cm^{-1} can be assigned to the OO stretching mode of peroxide species (O_2^{2-}). We also check the peaks in the range of 1500–1700 cm^{-1} , and the band at 1544 cm^{-1} could be clearly observed under oxygen flow, while an additional band at 1658 cm^{-1} appeared under ozone/oxygen flow. The band at 1544 cm^{-1} can be assigned to the molecular oxygen species and the new band at 1658 cm^{-1} is the overtone of the OO stretching vibration of the peroxide species because its wavenumber is almost twice that of the band at 835 cm^{-1} [22,50]. Similarly, the new peak occurred at 873 cm^{-1} when β - MnO_2 or γ - MnO_2 was exposed to ozone flow, which could be ascribed to the peroxide species. Meanwhile the overtone of peroxide at 1746 cm^{-1} was also observed. The above results indicate that over all three MnO_2 polymorphs, peroxide species are formed as an intermediate during ozone decomposition.

Furthermore, we also investigated the effect of reaction temperature on the peroxide species. As shown in Fig. 8, when the temperature increased from 25 $^{\circ}\text{C}$ to 60 $^{\circ}\text{C}$ and 100 $^{\circ}\text{C}$, the intensity of peroxide species over all three MnO_2 polymorphs decreased. However, the signal of peroxide species over α - MnO_2 reduced more significantly and almost disappeared at 100 $^{\circ}\text{C}$, while those over β - MnO_2 and γ - MnO_2 were less reduced. These results indicate that the decomposition of peroxide species was accelerated by increasing the reaction temperature, and its decomposition rate is consistent with the catalyst's activity. Thus, we conclude that the decomposition of peroxide species may be a rate-limiting step during ozone decomposition.

According to the above results and the ozone decomposition steps proposed in the literature [22], the ozone decomposition mechanism based on the involvement and recycling of oxygen vacancy is proposed. First, when ozone gas flows through MnO_2 , the ozone molecule binds to MnO_2 surface by inserting an O atom into an oxygen vacancy site. The oxygen vacancy is 2-electron donor and transfer 2-electron to an O atom of ozone [33,51], thus forming an oxygen species (O^{2-}) in the oxygen vacancy site and an oxygen molecule, which desorbs into the air (see (R2)). Then another ozone molecule reacts with O^{2-} to produce a gas-phase oxygen molecule and a bridging O_2 dimer (peroxide, O_2^{2-}), which was observed by in situ Raman spectroscopy (see (R3)). Finally, the peroxide species (O_2^{2-}) decomposes to release an oxygen molecule,

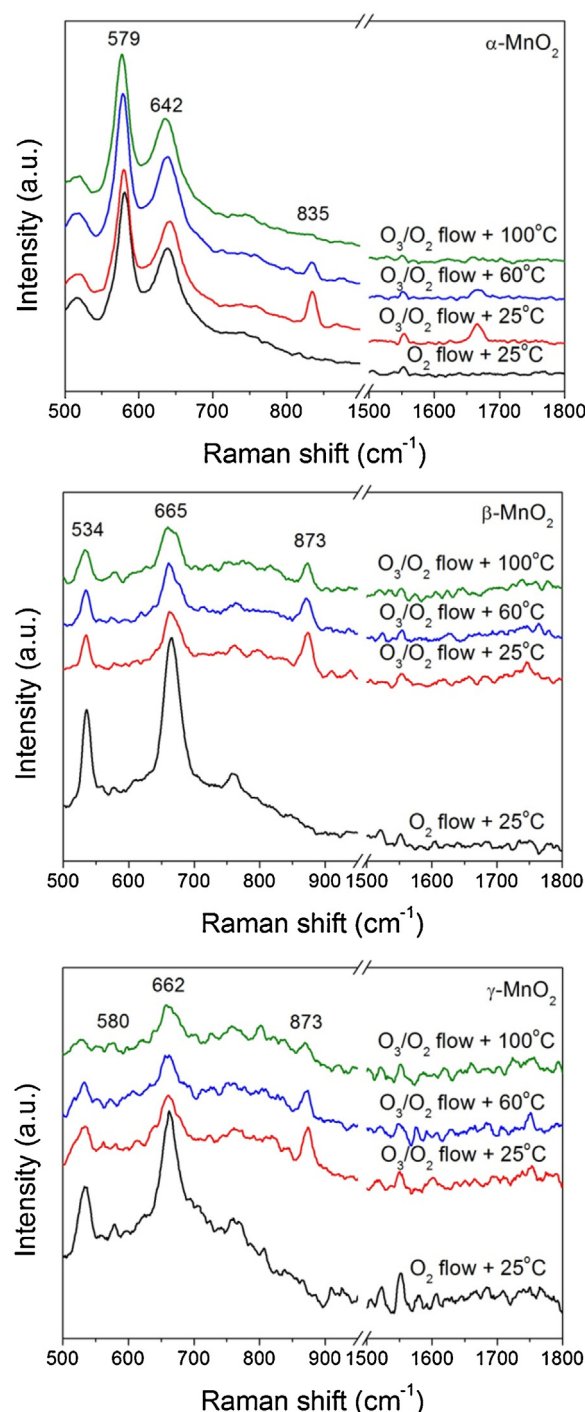


Fig. 8. In-situ Raman spectra of α -, β - and γ - MnO_2 treated under oxygen flow and oxygen/ozone mixture at different temperatures.

and consequently the oxygen vacancy is recovered (see (R4)), which can participate in the next cycle to decompose ozone.



According to this reaction mechanism, ozone decomposition rate i.e. the catalyst activity depends on the property and amount of the oxygen vacancy density [52]. Among three MnO_2 polymorphs tested in this research, α - MnO_2 owns the highest activity and

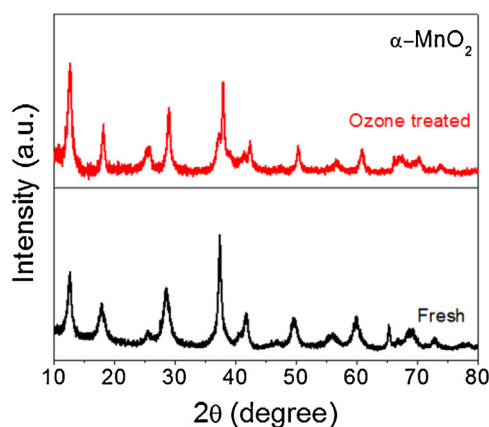


Fig. 9. XRD patterns of α - MnO_2 before and after treated with at ambient temperature for 99 h (ozone inlet concentration: 14 ppm, weight space velocity: $660 \text{ L g}^{-1} \text{ h}^{-1}$).

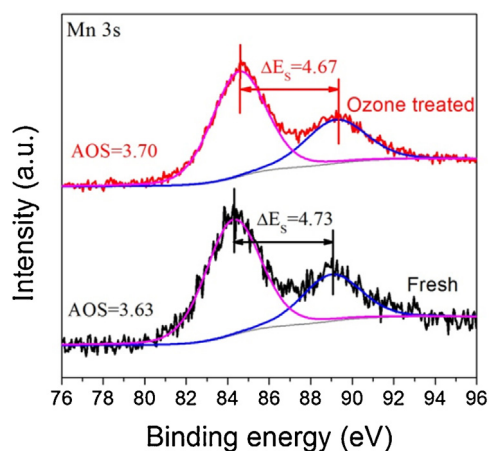


Fig. 10. Mn 3s XPS spectra of α - MnO_2 before and after treated with ozone at ambient temperature for 99 h (ozone inlet concentration: 14 ppm, weight space velocity: $660 \text{ L g}^{-1} \text{ h}^{-1}$).

oxygen vacancy density. The large amount of oxygen vacancy owned by α - MnO_2 can be ascribed to its largest specific surface area ($80.7 \text{ m}^2/\text{g}$) and its structure. In α - MnO_2 , the oxygen vacancies are more easily formed due to its longer Mn–O bond and weaker interaction between Mn and O atom as mentioned above. Besides, the catalyst activity also depends on the decomposition rate of intermediate oxygen species (O_2^- and O_2^{2-}). As revealed by in-situ Raman, peroxide species over α - MnO_2 decompose much faster than those over β - MnO_2 and γ - MnO_2 . On the contrary, if the decomposition of peroxide species is not sufficiently fast, the oxygen vacancy site will be occupied by intermediate oxygen species, or these intermediate oxygen species will transform into lattice oxygen [53]. As a result, the oxygen vacancy site can't be recovered, the average oxidation state of Mn increases, and the catalyst gradually loses its activity.

We investigated the change of the α - MnO_2 sample after it was used for ozone decomposition. The ozone removal ratio decreased from initial 100% to less than 80% after 99 h reaction at ambient temperature, indicating the catalyst partly deactivated. XRD analysis (Fig. 9) showed that it remained as α - MnO_2 structure after treated with ozone, as well as β - and γ - MnO_2 (Fig. S3), suggesting that the deactivation was not caused by the bulk phase transformation. However, Mn 3s XPS analysis (Fig. 10) indicated that the average oxidation state of Mn increased to 3.70 from 3.63 of untreated catalyst, confirming that some of Mn^{3+} was oxidized to Mn^{4+} during ozone decomposition reaction. In other words,

oxygen vacancies were not completely recovered, which resulted in gradual deactivation of catalyst.

4. Conclusions

Three kinds of manganese dioxide with different crystal structures, i.e., α -, β - and γ - MnO_2 were synthesized by hydrothermal method and tested for ozone decomposition. Among them, α - MnO_2 with (2×2) tunnel structure owns the largest specific surface area, lowest average Mn oxidation state, and the most abundant surface adsorbed oxygen species resulted from the oxygen vacancy sites. The formation of peroxide species over MnO_2 during ozone decomposition has been confirmed by in-situ Raman spectroscopy. It has also been observed that the peroxide species over α - MnO_2 can be more easily decomposed by increasing reaction temperature. The highest activity of α - MnO_2 toward ozone decomposition is ascribed to its highest oxygen vacancy sites and fast decomposition of peroxide species. Finally, the ozone decomposition mechanism based on the involvement and recycling of the oxygen vacancy is proposed.

Acknowledgments

This study was supported by the National High Technology Research and Development Program of China (2012AA062701), National Nature Science Foundation of China (21221004, 21411140032) and Tsinghua University Initiative Scientific Research Program (20131089251).

Appendix A. Supplementary data

Supplementary data associated with this article can be found, in the online version, at <http://dx.doi.org/10.1016/j.apcatb.2016.02.055>.

References

- [1] O.R. Cooper, D.D. Parrish, A. Stohl, M. Trainer, P. Nedelec, V. Thouret, J.P. Cammas, S.J. Oltmans, B.J. Johnson, D. Tarasick, T. Leblanc, I.S. McDermid, D. Jaffe, R. Gao, J. Stith, T. Ryerson, K. Aikin, T. Campos, A. Weinheimer, M.A. Avery, *Nature* 463 (2010) 344–348.
- [2] C.S. Kim, N.E. Alexis, A.G. Rappold, H. Kehrl, M.J. Hazucha, J.C. Lay, M.T. Schmitt, M. Case, R.B. Devlin, D.B. Peden, D. Diaz-Sanchez, *Am. J. Respir. Crit. Care Med.* 183 (2011) 1215–1221.
- [3] B. Hoffmann, H. Lüttmann-Gibson, A. Cohen, A. Zanobetti, C. de Souza, C. Foley, H.H. Suh, B.A. Coull, J. Schwartz, M. Middleman, P. Stone, E. Horton, D.R. Gold, *Environ. Health Perspect.* 120 (2012) 241–246.
- [4] J.D. Berman, N. Fann, J.W. Hollingsworth, K.E. Pinkerton, W.N. Rom, A.M. Szema, P.N. Breyse, R.H. White, F.C. Curriero, *Environ. Health Perspect.* 120 (2012) 1404–1410.
- [5] S. Avnery, D.L. Mauzerall, J. Liu, L.W. Horowitz, *Atmos. Environ.* 45 (2011) 2284–2296.
- [6] D. Shindell, J.C.I. Kuylenstierna, E. Vignati, R. van Dingenen, M. Amann, Z. Klimont, S.C. Anenberg, N. Müller, G. Janssens-Maenhout, F. Raes, J. Schwartz, G. Faluvegi, L. Pozzoli, K. Kupiainen, L. Hoeglund-Isaksson, L. Emberson, D. Streets, V. Ramanathan, K. Hicks, N.T.K. Oanh, G. Milly, M. Williams, V. Demkine, D. Fowler, *Science* 335 (2012) 183–189.
- [7] B. Stephens, E.T. Gall, J.A. Siegel, *Environ. Sci. Technol.* 46 (2012) 929–936.
- [8] M.G. Apte, I.S.H. Buchanan, M.J. Mendell, *Indoor Air* 18 (2008) 156–170.
- [9] I.S.H. Buchanan, M.J. Mendell, A.G. Mirer, M.G. Apte, *Indoor Air* 18 (2008) 144–155.
- [10] C.C.D. Fung, S. Shu, Y. Zhu, *Indoor Air* 24 (2014) 503–510.
- [11] A.C. Rai, C.-H. Lin, Q. Chen, *Atmos. Environ.* 102 (2015) 145–155.
- [12] E. Rezaei, J. Soltan, *Appl. Catal. B: Environ.* 148 (2014) 70–79.
- [13] H. Einaga, N. Maeda, Y. Teraoka, *Appl. Catal. B: Environ.* 142–143 (2013) 406–413.
- [14] H. Einaga, S. Yamamoto, N. Maeda, Y. Teraoka, *Catal. Today* 242 (2015) 287–293.
- [15] J. Nawrocki, B. Kasprzyk-Hordern, *Appl. Catal. B: Environ.* 99 (2010) 27–42.
- [16] J.S. Ebrahim Rezaei, Ning Chen, *Appl. Catal. B: Environ.* 136–137 (2013) 239–247.
- [17] J.V. Durme, J. Dewulf, K. Demeestere, C. Leys, H.V. Langenhove, *Appl. Catal. B: Environ.* 87 (2009) 78–83.
- [18] U. Roland, F. Holzer, F.-D. Kopinke, *Appl. Catal. B: Environ.* 58 (2005) 217–226.
- [19] H. Huang, H. Huang, Y. Zhan, G. Liu, X. Wang, H. Lu, L. Xiao, Q. Feng, D.Y.C. Leung, *Appl. Catal. B: Environ.* 186 (2016) 62–68.

- [20] Z.P. Hao, D.Y. Cheng, Y. Guo, Y.H. Liang, *Appl. Catal. B: Environ.* 33 (2001) 217–222.
- [21] W. Li, S.T. Oyama, *J. Am. Chem. Soc.* 120 (1998) 9047–9052.
- [22] W. Li, G.V. Gibbs, S.T. Oyama, *J. Am. Chem. Soc.* 120 (1998) 9041–9046.
- [23] S.M. Saqer, D.I. Kondarides, X.E. Verykios, *Appl. Catal. B: Environ.* 103 (2011) 275–286.
- [24] B. Dhandapani, S.T. Oyama, *Appl. Catal. B: Environ.* 11 (1997) 129–166.
- [25] C. Heisig, W.M. Zhang, S.T. Oyama, *Appl. Catal. B: Environ.* 14 (1997) 117–129.
- [26] C. Subrahmanyam, D.A. Bulushev, L. Kiwi-Minsker, *Appl. Catal. B: Environ.* 61 (2005) 98–106.
- [27] C. Jiang, P. Zhang, B. Zhang, J. Li, M. Wang, *Ozone: Sci. Eng.* 35 (2013) 308–315.
- [28] M. Wang, P. Zhang, J. Li, C. Jiang, *Chin. J. Catal.* 35 (2014) 335–341.
- [29] B. Dhandapani, S.T. Oyama, *Chem. Lett.* (1995) 413–414.
- [30] C.Y.H. Chao, C.W. Kwong, K.S. Hui, *J. Hazard. Mater.* 143 (2007) 118–127.
- [31] S. Alejandro, H. Valdes, C.A. Zaror, *J. Adv. Oxid. Technol.* 14 (2011) 182–189.
- [32] N. Brodu, M.-H. Manero, C. Andriantsiferana, J.-S. Pic, H. Valdes, *Chem. Eng. J.* 231 (2013) 281–286.
- [33] R. Radhakrishnan, S.T. Oyama, J.G.G. Chen, K. Asakura, *J. Phys. Chem. B* 105 (2001) 4245–4253.
- [34] R. Radhakrishnan, S.T. Oyama, *J. Catal.* 199 (2001) 282–290.
- [35] S.S. Kim, S.C. Hong, K.H. Han, *Ozone: Sci. Eng.* 35 (2013) 514–518.
- [36] T. Kameya, K. Urano, *J. Environ. Eng. ASCE* 128 (2002) 286–292.
- [37] F. Cheng, Y. Su, J. Liang, Z. Tao, J. Chen, *Chem. Mater.* 22 (2010) 898–905.
- [38] Y. Zhang, C. Sun, P. Lu, K. Li, S. Song, D. Xue, *CrystEngComm* 14 (2012) 5892–5897.
- [39] B. Bai, J. Li, J. Hao, *Appl. Catal. B: Environ.* 164 (2015) 241–250.
- [40] S. Liang, F.T.G. Bulgan, R. Zong, Y. Zhu, *J. Phys. Chem. C* 112 (2008) 5307–5315.
- [41] F. Shi, F. Wang, H. Dai, J. Dai, J. Deng, Y. Liu, G. Bai, K. Ji, C.T. Au, *Appl. Catal. A: Gen.* 433 (2012) 206–213.
- [42] F. Wang, H. Dai, J. Deng, G. Bai, K. Ji, Y. Liu, *Environ. Sci. Technol.* 46 (2012) 4034–4041.
- [43] Y. Xie, Y. Yu, X. Gong, Y. Guo, Y. Guo, Y. Wang, G. Lu, *CrystEngComm* 17 (2015) 3005–3014.
- [44] Y. Yang, J. Huang, S. Wang, S. Deng, B. Wang, G. Yu, *Appl. Catal. B: Environ.* 142 (2013) 568–578.
- [45] C. Wang, L. Sun, Q. Cao, B. Hu, Z. Huang, X. Tang, *Appl. Catal. B: Environ.* 101 (2011) 598–605.
- [46] J. Luo, Q. Zhang, J. Garcia-Martinez, S.L. Suib, *J. Am. Chem. Soc.* 130 (2008) 3198–3207.
- [47] T. Gao, H. Fjellvag, P. Norby, *Anal. Chim. Acta* 648 (2009) 235–239.
- [48] T. Gao, H. Fjellvag, P. Norby, *Nanotechnology* 20 (2009).
- [49] X.-L. Jing, Q.-C. Chen, C. He, X.-Q. Zhu, W.-Z. Weng, W.-S. Xia, H.-L. Wan, *Phys. Chem. Chem. Phys.* 14 (2012) 6898–6904.
- [50] W.Z. Weng, H.L. Wan, J.M. Li, Z.X. Cao, *Angew. Chem. Int. Ed.* 43 (2004) 975–977.
- [51] M. Setvin, U. Aschauer, P. Scheiber, Y.-F. Li, W. Hou, M. Schmid, A. Selloni, U. Diebold, *Science* 341 (2013) 988–991.
- [52] J.M. López, A.L. Gilbank, T. García, B. Solsona, S. Agouram, L. Torrente-Murciano, *Appl. Catal. B: Environ.* 174–175 (2015) 403–412.
- [53] G.I. Panov, K.A. Dubkov, E.V. Starokon, *Catal. Today* 117 (2006) 148–155.